Development of Turbulence Diagnostics on Three-Dimensional Fields Obtained by Numerical Simulations in Magnetically Confined Plasmas

N. Kasuya 1), S. Nishimura 1), M. Yagi 2), K. Itoh 1), S.-I. Itoh 2) and N. Ohyabu 1)

1) National Institute for Fusion Science, Toki, Gifu 509-5292, Japan
2) Research Institute for Applied Mechanics, Kyushu University, Kasuga, Fukuoka 816-8580, Japan

e-mail contact of main author: kasuya@nifs.ac.jp

Abstract. It is important to clarify the role of turbulent structures on anomalous transport in fusion plasmas. We have been developing a turbulence diagnostic simulator to promote collaboration between numerical simulations and experiments by progressing the e-science. For the study of structural formation in helical plasmas, the spatio-temporal data of turbulent fields are generated by global simulation using a reduced MHD model describing drift-interchange instability. Numerical diagnostics simulating turbulence diagnostics in experiments, such as a heavy ion beam probe and phase contrast imaging, are carried out on the time series data for quantitative comparison. Next, elemental processes of mode couplings are studied in detail in the simple cylindrical configuration. Three kinds of turbulent structures, i.e., zonal flow, streamer, solitary vortex, have been obtained in the nonlinear simulation of the resistive drift wave turbulence, and spectral analyses show the characteristic feature of each structure. The analyses provide a test to verify the appropriateness of spatial resolution, and give quantitative interpretation of observed signals, which deepen our physical understanding of self-sustained structural formation mechanism.

1. Introduction

Turbulent plasmas form a variety of nonlinear structures [1,2]. The theoretical researches reveal formation of meso-scale structures by interaction of various modes with different scales, which affects the level of turbulent transport. Therefore, it is important to clarify the role of the turbulent structures on anomalous transport in fusion plasmas. Progress in experimental techniques of high resolution measurements enables to make quantitative estimation of turbulence transport [3,4]. Detailed measurements in laboratory plasma reveal the turbulent structure [5-7]. Some diagnostics have detected the characteristic feature of turbulence [8-11], however, measurements in large devices are limited, so improvement of the data analysis technique is necessary to obtain the maximum information from experimental data.
We have been developing a turbulence diagnostic simulator (TDS), which simulates plasma turbulence numerically [12]. Data analyses as same in the experiments are carried out on the simulation data [13] for quantitative comparison, taking account of the plasma configuration, physical mechanism of diagnostics and finite spatial resolution. In this paper, numerical diagnostics in helical and cylindrical plasmas are carried out using the TDS.

2. Turbulence Diagnostic Simulator

For turbulence analyses, we have been developing the assembly of codes, named ‘turbulence diagnostic simulator’ (TDS). The TDS consists of two main parts; turbulence codes and modules simulating experimental diagnostics. The schematic of data flow in the TDS is shown in Fig. 1. Turbulent fields are produced by fluid simulations using a supercomputer. Calculations in several kinds of magnetic configurations, such as helical, tokamak and linear devices, are carried out, and time series data of three-dimensional (3-D) fluctuation fields are obtained. The data are transferred to a data storage. A large number of temporal points, which are sufficient for statistical analyses, are stored, so the data size is

the order of tera-bytes in the case of toroidal plasmas. The stored data are analyzed using modules to simulate experimental diagnostics of turbulence, such as HIBP, PCI and an electrostatic probe, and produce results that can be compared with experiments. The TDS includes the several turbulence codes and the several numerical measurement modules. The combination is selected in accordance with the research object.

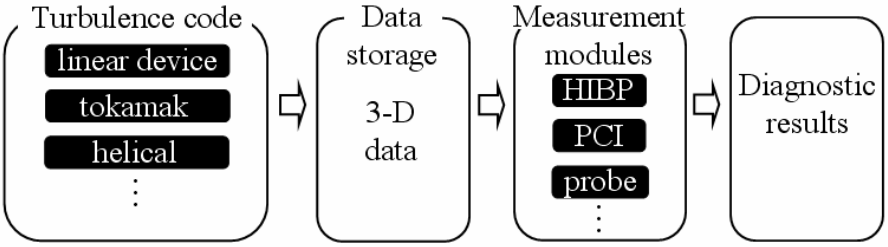

FIG 1. Schematic of data flow in the turbulence diagnostic simulator

3. Numerical Diagnostics

We have been developing the turbulence diagnostic simulator in helical plasmas. Several modules simulating experimental diagnostics are available for analyses of time series of 3-D data from turbulent simulations. Here, analyses with a HIBP and PCI module are described.

3.1. Drift-interchange mode turbulence in helical plasmas

To provide turbulence data, the simulation code has been extended to calculate the drift-interchange turbulence in helical plasmas with a circular cross-section. The averaging method with the stellarator expansion [14,15] is applied to give a set of model equations as

$$\frac{\partial \nabla_\perp^2 u}{\partial t} = \left[u, \nabla_\perp^2 u\right] + \nabla_{//} \nabla_\perp^2 A + \left[\Omega, P\right] + \mu \nabla_\perp^4 u, \quad (1)$$

$$\frac{\partial A}{\partial t} = \nabla_{//} \left(u + \alpha P\right) + \eta \nabla_\perp^2 A, \quad (2)$$

$$\frac{\partial P}{\partial t} = \left[u, P\right] - C \nabla_{//} \nabla_\perp^2 A + \eta_\perp \nabla_\perp^2 P + S, \quad (3)$$

where u is the stream function, A is the ζ component of the vector potential, P is the total pressure. The details of the model are described in [16]. This model corresponds to the resistive interchange model with the extension to include the parallel dynamics.

The nonlinear simulation has been performed, using the following parameters: magnetic field B = 2.0 [T], electron temperature T_e = 1 [keV], minor radius a = 0.6 [m], major radius R_0 = 3.75 [m], viscosities $\mu = \eta = \eta_\perp = 1 \times 10^{-5}$, pole number l = 2, pitch number M = 10. Rotational transform ι is given to be a monotonically increasing function with the radius from $\iota(0) = 0.41$ to $\iota(1) = 1.17$. 1024 grids in the radial direction and Fourier modes $-64 \le m \le 64$, $-16 \le n \le 16$ are taken in simulations, where m and n are the poloidal and toroidal mode number, respectively.

Spatio-temporal data of turbulent fields are generated by this global simulation. Figure 2 (a) shows the time evolutions of the fluctuating energy of the electrostatic potential. Low m, n modes are excited in the linear growing phase, and saturation is obtained with energy exchange between various modes by nonlinear couplings. Figure 2 (b) shows the energy spectrum of the electrostatic potential on m in the nonlinear saturation state. The snapshots of the contours of the fluctuations at t = 1000 are shown in Fig. 3. Here, we assumed that variables u and P represent the normalized electrostatic potential and density, respectively.

3.2. Numerical heavy ion beam probe

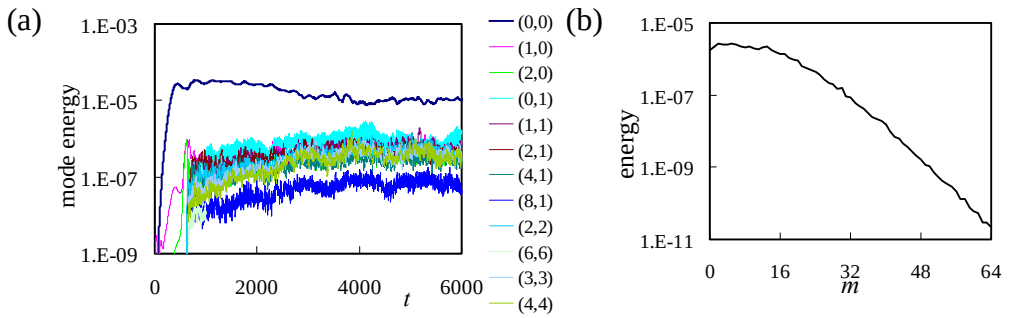

FIG. 2. (a) Time evolutions of the electrostatic potential energy of Fourier modes. (b) Potential energy spectrum on poloidal mode number m in the nonlinear saturation state.

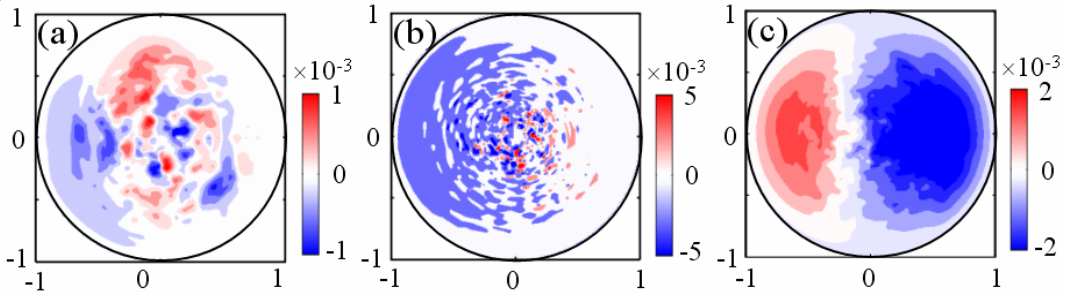

FIG. 3. Contours of (a) the electrostatic potential, (b) density and (c) vector potential fluctuation on the poloidal cross-section. These are the snapshots at t = 1000 in Fig. 2.

The HIBP is used for the measurement of the electrostatic potential and density in the core plasmas [17,18]. A HIBP module simulates the measurement as the following way [16]; the injection point, angle, energy, and detector position are set at first, and the trajectories of the injected ions are calculated in the fluctuating fields using the equation of motion. The charges of the ions are changed from +1 to +2 on the way to find the ionization point, from which the ions get into the detector position. The detector catches ions from some region in accordance with the finite beam width and detector size. The energies of ions and the beam intensity [19] are calculated, and averaged over the ionization region (sample volume) to give HIBP signals taking account of the spatial resolutions. Note that if the density is low, the attenuation along the trajectory is small and the beam intensity can be assumed to obey the density at the ionization point. According to experiments [10], singly ionized gold ions (Au^+) are injected with the energy of 1.5 [MeV] as a probing beam.

Radial profiles are calculated using the snapshot data of the potential and density in Fig. 3. Figure 4 shows the numerically measured values and the local values at the center of the sample volume. Comparison between them indicates that the calculated values agree well in the potential case, but large deviation exists in the density case. This is because the HIBP signal is given by averaging over the sample volume. As is shown in Fig. 3, the typical length of the fluctuations is larger in the potential than in the density. So the averaging screens the fine structures, which gives the large deviation in the density measurement.

The data has time series, so time evolutions of quantities can be obtained. Figure 5 shows the time evolutions of (a) the potential, (b) detected beam intensity, (c) observation point and (d) size of the sample volume. These values are obtained by analyzing the fluctuation data with fixed injection and detection conditions. Figure 5 (c) indicates that the deviation of the observation point is 5 % at most. In addition to that, Fig. 5 (d) indicates that the size of the sample volume is around 8 % of the radius. Therefore, the potential and density fluctuations have the deviation of more than 10 % from the values at the fixed position in the sample volume. The spatial resolution necessary to resolve the target fluctuation can be estimated with this numerical measurement.

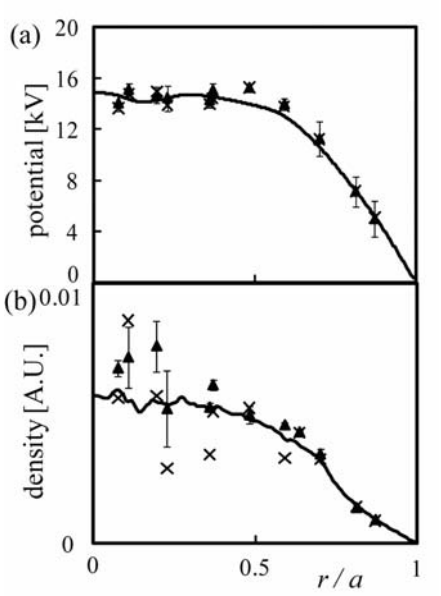

FIG. 4. Measurements of (a) the electrostatic potential and (b) density by using the numerical HIBP on the fluctuating field in Fig. 3. Triangles (▲), crosses (×) and the solid line (-) indicate the numerical measurements, corresponding local values and the mean profile, respectively.

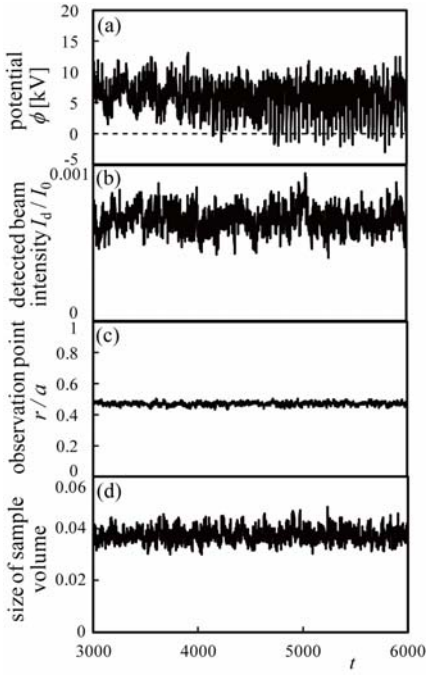

FIG. 5. Time evolutions of (a) the electrostatic potential, (b) detected beam intensity, (c) observation point and (d) size of the sample volume from the numerical HIBP measurement.

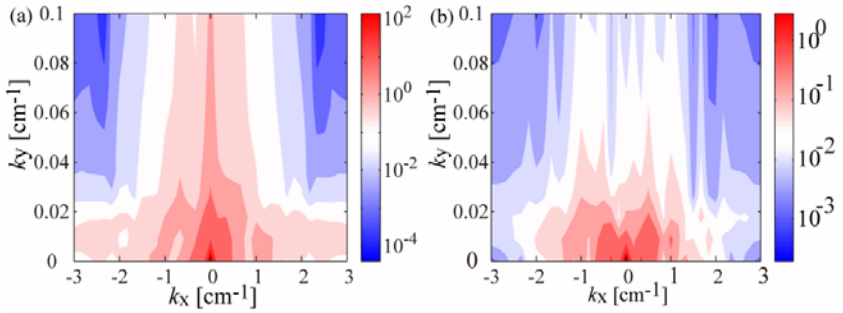

FIG. 6. 2-D k spectra of (a) the line integrated and (b) local density fluctuation at z = 0. These are obtained from the fluctuation field including all mode calculated in the simulation.

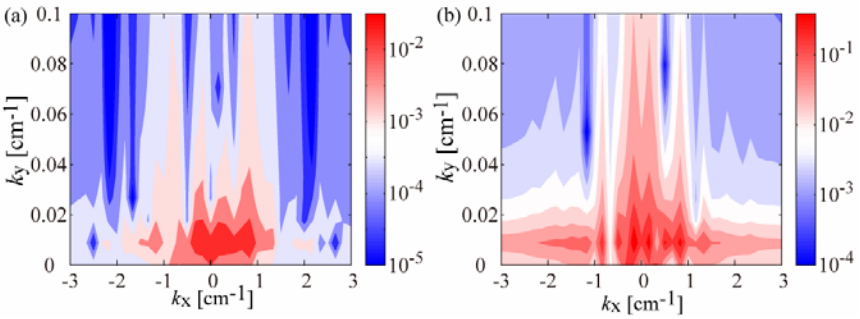

FIG. 7. 2-D k spectra of (a) the line integrated and (b) local density fluctuation at z = 0. These are obtained from the fluctuation field including only (m, n) = (30, 12) and its complex conjugate.

3.3. Numerical phase contrast imaging

The PCI is used for the measurement of density fluctuation with high temporal and wave number resolutions [20,21]. An injected laser beam is scattered by the density fluctuation, and interference between the scattered and unscattered reference beam gives the two-dimensional (2-D) pattern of the fluctuation in the *k* space. The signals are given as the

integral of the density fluctuation along the line of sight, so there is a problem to resolve the local values from the signals. The pitch angle of the magnetic field helps the identification [20]. Here we obtained the 2-D spectrum of the density fluctuation using the simulation data, and compare those from local fluctuation and integration along the beam path.
Time series data for t = 3000 - 4000 in Fig. 2 is used for the numerical analyses. The beam is injected vertically, and the fluctuations at $R = R_0 + 0.5a$ and ζ =0 are calculated. Figure 6 shows the 2-D wave number spectra of (a) the line integrated and (b) local density fluctuation at z = 0, where z is the distance from the midplane, k_x and k_y is the wave number in the R and ζ direction, respectively. Low k_x modes ($|k_x| < 1$ [cm^{-1}]) exist, and the broad band spectrum makes it difficult to identify the local fluctuations.
Next we subtract the single mode (m, n) = (30, 12) and its complex conjugate from the turbulence data, and calculate the 2-D wave number spectrum (Fig. 7). Only the n = 12 mode is included, so there is the peak at $k_y = 9 \times 10^{-3}$ [cm^{-1}]. Wave number k_x is given by combination of k_r and k_θ, and k_r is dominant in this case, so several peaks exist in the k_x spectrum. The correlation between the integrated and local signals is calculated to subtract the local information from the integrated signal. The peak of the correlation exists at k_x = 0.67, 0.33 and 0.17 [cm^{-1}] with z = 0, 0.2a and 0.4a, respectively. This dependence comes from the smaller projection of k_r on the x direction at larger z. In this way, simulation data can be used as a test field for interpretation of the measured signals.

4. Focused Investigation on Elementary Processes

Turbulence diagnostics are carried out using the TDS. Next, elementary processes of mode couplings are studied in the simple cylindrical configuration. Several kinds of turbulent structures are obtained, and numerical measurements show their characteristic feature.

4.1. Resistive drift wave turbulence in cylindrical plasmas

Plasma experiments in a simple linear configuration have been revisited for quantitative understandings of the structural formation mechanism by turbulence [5-7]. These laboratory plasmas are suitable for carrying out detailed measurements. We have been developing a 3-D numerical simulation code of the resistive drift wave turbulence in a linear device, called ‘Numerical Linear Device’ (NLD) [22]. The three-field (density N, potential ϕ and parallel velocity of electrons V) reduced fluid model is adopted, and the continuity equation, the vorticity equation and Ohm's law give the following set of model equations:

$$\frac{dN}{dt} = -\nabla_{//}V - V\nabla_{//}N + \mu_N\nabla_\perp{}^2 N + S, \tag{4}$$

$$\frac{d\nabla_\perp{}^2\phi}{dt} = \nabla N\cdot\left(-\nu_{in}\nabla_\perp\phi - \frac{d\nabla_\perp\phi}{dt}\right) - \nu_{in}\nabla_\perp{}^2\phi - \nabla_{//}V - V\nabla_{//}N + \mu_W\nabla_\perp{}^4\phi, \tag{5}$$

$$\frac{dV}{dt} = \frac{M}{m_e}\left(\nabla_{//}\phi - \nabla_{//}N\right) - \nu_e V + \mu_V\nabla_\perp{}^2 V. \tag{6}$$

The details of the model are described in [22]. The density of neutral particles is high even in the plasma core region [23], so the effect of neutral particles is taken into consideration. The equations are solved in the cylindrical coordinate with spectral expansion in the azimuthal and axial directions.
Nonlinear simulations have been performed, using the following parameters: magnetic field B = 0.1 [T], electron temperature T_e = 2 [eV], plasma radius a = 10 [cm], length of the device λ = 1.7 [m], viscosities $\mu_N = 1 \times 10^{-2}$, $\mu_V = \mu_W = 1 \times 10^{-4}$, electron collision frequency ν_e = 310. The electron collisions (ν_e) destabilize and the ion-neutral collisions

(ν_{in}) stabilize the resistive drift wave. There is ambiguity of the value of collision frequency ν_{in}, which depends on the neutral density. Therefore, ν_{in} is used as a parameter for controlling the instability in our simulations. The calculation with a fixed particle source, which forms a density profile peaked at r = 0, has been carried out. Simulations are performed with 256 grids in the radial direction, and Fourier modes (m, n) = (0, 0) and m = ±1 - ±16, n = ±1 - ±16 are taken.

4.2. Turbulent structures

Using NLD, selective formation of the turbulent structures has been studied [24]. In the nonlinear saturation states, several kinds of turbulent structures have been obtained. If the collision frequency is small, compared with the growth rate of unstable modes in saturated states, modulational coupling of unstable modes generates the (0, 0) mode, which is the zonal flow (Fig. 8 (a)). The perturbation structure in the zonal flow case is a mixture of some modes (Fig. 8 (b)). The amplitude of the (0, 0) mode oscillates, and those of the other modes varies, accordingly. The limit cycle oscillation between the (0, 0) mode and the perturbations contributes to the saturation [25].
If the collision frequency is large, the zonal flow remains stable, owing to strong collisional damping, and parametric coupling with modes, which have neighboring m and the frequency close to each other, forms a streamer (Fig. 8 (c)). Strong vortex is localized in the poloidal direction, and rotates to the electron diamagnetic direction. The localized structure is sustained for much longer duration than the typical time scale of the drift wave oscillation (more than 3000 Ω_{ci}^{-1}). Modes with (m, n) = (±4, ±1) and (±5, ±1) are dominant in this case, and their nonlinear coupling and self-bunching with the mediator mode (1, 2) is the origin of the sustainment of the streamer [24]. This prediction has guided the experimental discovery of the streamer on the experimental device LMD-U [5].
The energy exchange for streamer formation is selected, if the neighboring m modes are unstable [26]. However, in the case when a single mode is unstable, we found the nonlinear saturation with a solitary vortex (modon, dipole solitary vortex solution of the nonlinear drift wave [27]). The particle source, which shifts the steep gradient region of the density inward to the plasma center, changes the dependency of the linear growthrate on m, and the saturation state with the single dominant mode and its higher harmonics is obtained (Fig. 8 (d)). The (2, 1) mode is dominant, and self-bunching steepens the structure, which is one of the candidates of the solitary vortex.

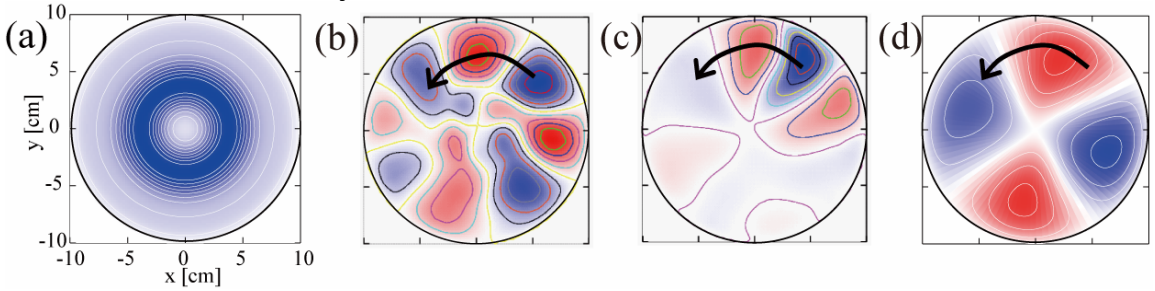

FIG. 8. Snapshots of the contour of the electrostatic potential, which is normalized by the maximum value at that time. The typical structure in the zonal flow case and its perturbed component, that in the streamer case and the solitary vortex case are shown in (a) - (d), respectively. The structures rotate in the electron diamagnetic direction, as indicated with the arrows.

4.3. Multiple probe measurement

In laboratory plasma experiments, the electrostatic probe measurement is useful to obtain fluctuation data with high spatial and temporal resolutions [5]. We carry out analyses

resemble to the multi probe measurements on the time series of 3-D fields to identify the difference of the turbulent structures in the previous subsection [12].
The correlation between two radial points is analyzed. This corresponds to the analysis using two probe signals at different radii. Figure 9 shows the temporal evolutions of the radial correlation of potential fluctuations between r / a = 0.5 and 0.75. In the streamer case, the radial correlation becomes close to 1, when the streamer comes to the observation point, t ~ 5700. In the zonal flow case, the radial correlation is smaller than that in the streamer case. There is a duration when the correlation becomes close to 1 even in the zonal flow case. The streamer like structure appears intermittently, but is sustained only for a short duration, so temporally averaged correlation is smaller than that in the streamer case. In the solitary vortex case, the radial correlation is close to 1 for the whole duration. This is because the single dominant mode is steadily sustained, and the amplitudes of the higher harmonics are comparably small.
A poloidal probe array gives the spatio-temporal structures. 2-D Fourier decomposition of time series data of the poloidal profiles gives the spatio-temporal spectrum of the potential as in the probe array measurement (Fig. 10). In the zonal flow case, low m modes with weak dispersion, which are linearly unstable, are excited and show the broad band spectrum. Frequencies of the dominant modes are close to each other, and their harmonics are excited in the streamer case. The rather coherent spectrum appears in this case. The dispersion relation satisfies the theoretical relation of excited modes with nonlinear coupling [28]. In the solitary vortex case, the single unstable mode has large amplitude, and its higher harmonics are excited coherently. In this way, the spatio-temporal spectra show clear difference between the formed structures.

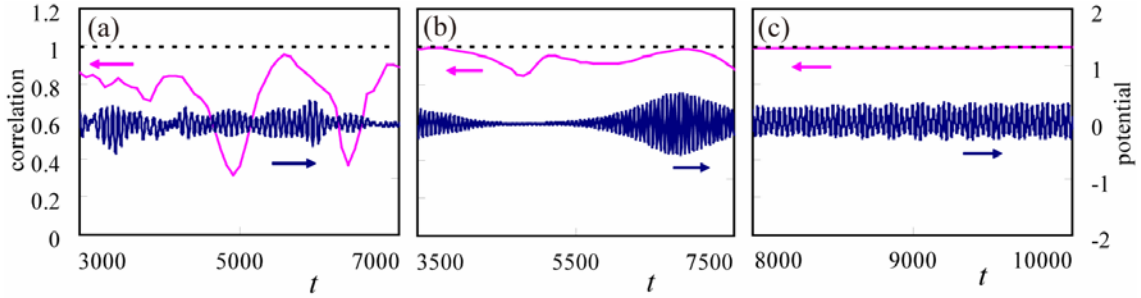

FIG. 9. Time evolutions of the radial correlation of the potential fluctuations between r / a = 0.5 and 0.75 in (a) the zonal flow, (b) streamer and (c) solitary vortex case.

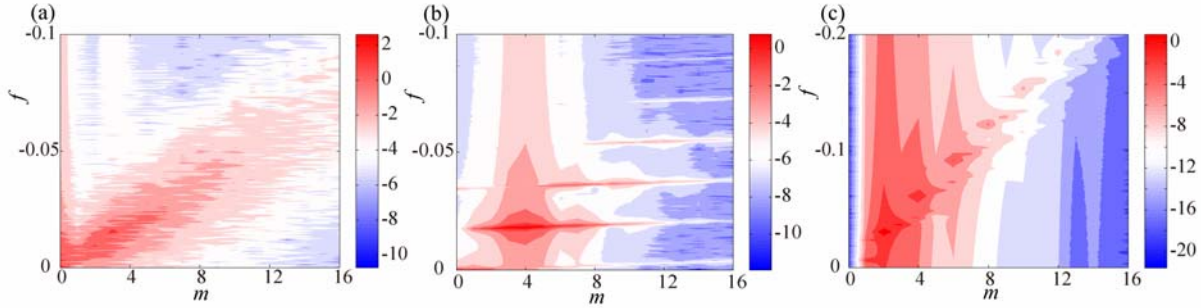

FIG. 10. Spatio-temporal spectra in (a) the zonal flow, (b) streamer and (c) solitary vortex case.

5. Summary

We have been developing the turbulence diagnostic simulator, which is the assembly of several turbulence codes and modules simulating experimental diagnostics. Turbulence codes in magnetized plasmas, such as helical and linear devices, produce time series of 3-D turbulence data, on which data analyses as same in the experiments are carried out. The

spatio-temporal data of turbulent fields are generated by global simulation in helical plasmas, and numerical diagnostics simulating turbulence diagnostics, such as a heavy ion beam probe and phase contrast imaging, are carried out on the data. Numerical diagnostics in cylindrical plasmas clarified elemental processes of turbulent structural formation. Three kinds of turbulent structures, i.e., zonal flow, streamer, solitary vortex, have been obtained in the nonlinear simulations, and the spectral analyses show their characteristic feature.
The numerical diagnostics provide a test field for quantitative interpretation of observed signals. Integration of several measurement modules accelerates comparison over the wide range in space and time. The turbulence diagnostic simulator will be used as a tool to promote collaboration of numerical simulations and experiments.

Acknowledgements

Authors acknowledge discussions with Prof. A. Fujisawa, Prof. K. Ida, Prof. A. Fukuyama, Dr. S. Inagaki, Dr. Y. Nagashima, and Dr. T. Yamada. This work is supported by the Grant-in-Aid for Young Scientists (20760581) and for Scientific Research (19360418, 21224014) of JSPS, by the collaboration program of NIFS (NIFS09KTAD009, NIFS09KDAD009, NIFS10KLHH315) and of RIAM of Kyushu University.

---

[1] See reviews, e.g. DIAMOND, P. H., *et al.*, Plasma Phys. Control. Fusion **47** (2005) R35.
[2] YOSHIZAWA, A., ITOH, S.-I., and ITOH, K., *Plasma and fluid turbulence* (IOP Publishing, Bristol, 2003).
[3] FUJISAWA, A., Nucl. Fusion **49** (2009) 013001.
[4] TYNAN, G. R., *et al.*, Plasma Phys. Control. Fusion **51** (2009) 113001.
[5]YAMADA, T., *et al.*, Nature Phys. **4** (2008) 721.
[6] ANTAR, G. Y., YU, J. H. and TYNAN, G. R., Phys. Plasmas **14** (2007) 022301.
[7] WINDISCH, T., GRULKE, O. and KLINGER, T., Phys. Plasmas **13** (2006) 122303.
[8] POLITZER, P. A., Phys. Rev. Lett. **84** (2000) 1192.
[9] CONWAY, G. D., Plasma Phys. Control. Fusion **50** (2008) 124026.
[10] IDO, T., *et al*., Plasma Sci. Technol. **11** (2009) 460.
[11] INAGAKI, S., *et al*., submitted to Phys. Rev. Lett.
[12] KASUYA, N., *et al.*, J. Plasma Fusion Res. SERIES **9** (2010) 523.
[13] NISHIMURA, S., *et al*., Plasma Fusion Res., in press.
[14] GREEN, J. M. and JOHNSON, J. L., Phys. Fluids **4** (1961) 875.
[15] WAKATANI, M., *Stellarator and Heliotron Devices* (Oxford University Press, Oxford 1998).
[16] KASUYA, N., *et al.*, submitted to Plasma Sci. Tech.
[17] CROWLEY, T. P., IEEE Trans. Plasma Sci. **22** (1994) 291.
[18] FUJISAWA, A., *et al*., Phys. Rev. Lett. **93** (2004) 165002.
[19] NAKANO, H., *et al.*, Rev. Sci. Instrum. **78** (2007) 063502.
[20] LIN, L., *et al.*, Phys. Plasmas **16** (2009) 012502.
[21] TANAKA, K., *et al.*, Nucl. Fusion **46** (2006) 110.
[22] KASUYA, N., *et al*., J. Phys. Soc. Jpn. **76** (2007) 044501.
[23] IGNATENKO, M., *et al.*, Jpn. J. Appl. Phys. **46** (2007) 1680.
[24] KASUYA, N., YAGI, M., ITOH, K. and ITOH, S.-I., Phys. Plasmas **15** (2008) 052302.
[25] KASUYA, N., *et al.*, J. Phys.: Conference Series **123** (2008) 012026.
[26] KASUYA, N., *et al.*, J. Plasma Fusion Res. SERIES **8** (2009) 77.
[27] LARICHEV, V. D. and REZNIK, G. M., Dokl. Akad. Nauk SSSR **231** (1976) 1077.
[28] ITOH, S.-I. and ITOH, K., J. Phys. Soc. Jpn **78** (2009) 124502.